sciendo

CAIM
ISSN 2038-0909

Commun. Appl. Ind. Math. 16 (1), 2025, 1–18 DOI: 10.2478/caim-2025-0001

Research Article

Special properties of transonic flows in a channel with a lenticular bump

Renato Paciorri[1], Alessia Assonitis[1*], Aldo Bonfiglioli[2]

[1]Dept. of Mechanical and Aerospace Engineering, University of Rome "La Sapienza", Rome, Italy

[2]Department of Engineering, University of Basilicata, Potenza, Italy

[*]Email address for correspondence: alessia.assonitis@uniroma1.it

Communicated by Enrico De Bernardis

Received on 02 28, 2024. Accepted on 09 24, 2024.

Abstract

The present study focuses on particular properties of transonic flows through a planar channel featuring a circular bump on the lower wall. The selected geometry is reminiscent of the region surrounding the trailing edge of an airfoil at zero angle of attack and the resulting flow pattern is indeed similar to the fishtail shock-pattern that characterizes airfoils flying at nearly sonic speed. Numerical simulations have been conducted by solving the inviscid Euler equations using both a commercial and an in-house CFD code; discontinuities are modeled using shock-capturing in the former and shock-fitting in the latter. Numerical experiments reveal different shock-patterns obtained by independently varying the inlet Mach number and the outlet-to-inlet static pressure ratio. When shock-interactions occur, shock-polar analysis reveals that the branching point can be modeled using either von Neumann's three-shock-theory or Guderley's four-wave-theory, depending on the inlet Mach number. Furthermore, for certain pairs of boundary conditions, multiple solutions have been observed.

Keywords: `Shock waves, shock-fitting, von Neumann's model, Guderley's model`

AMS subject classification: `76-10 - Mathematical modeling or simulation for problems pertaining to fluid mechanics`

1. Introduction

The transonic flow regime, which is characterized by the coexistence of subsonic and supersonic flow regions, is a common occurrence in both external and internal aerodynamics and has therefore been the subject of several theoretical, numerical and experimental studies [1–5]. Airfoil design in the transonic regime aims at reducing shock-induced drag losses, which requires full understanding of the effect that boundary conditions, such as the free-stream Mach number, M_∞, angle of attack and airfoil shape, play upon the flow structure.

In previous studies [6,7], the authors analyzed the so-called "fishtail" shock-pattern the characterizes the transonic flow past a NACA0012 airfoil at zero incidence and for M_∞ ranging between 0.91 to 0.95. Figure 1a, which is taken from the video-documentary "High Speed Flight: Part 2 - Transonic Flight", produced by the Shell Film Unit in 1959 [8] shows an experimental visualization of the fishtail shock-pattern. It consists in two oblique shock waves that originate at the trailing edge (TE) of the airfoil and a nearly normal shock standing behind the TE; the two oblique shocks and the normal shock merge at two branching points (circled using a white solid line in Fig. 1a) which resemble the triple-point that is observed in steady and un-steady Mach reflections. Mach reflections can be modeled using von Neumann's three-shock theory [9,10] (3ST) except when the two parameters that characterize the interaction fall inside the so-called von Neumann region [11], in which case the experimental evidence reveals a triple-point structure that the 3ST fails to predict. This inconsistency has been dubbed the "von Neumann paradox" by Birkhoff [12] in the 1950s and has since been the subject of several theoretical, experimental and numerical investigations, see e.g. [13,14]. One way to reconcile theory and experiments under the "von Neumann paradox" conditions consists in postulating the existence of a fourth wave, an expansion fan, also centred at the branching point. This four-wave theory (4WT) is known in the literature as Guderley's model [15]; according to [16], the 4WT solves the von Neumann paradox, at least

in the limit of vanishing viscosity [17].

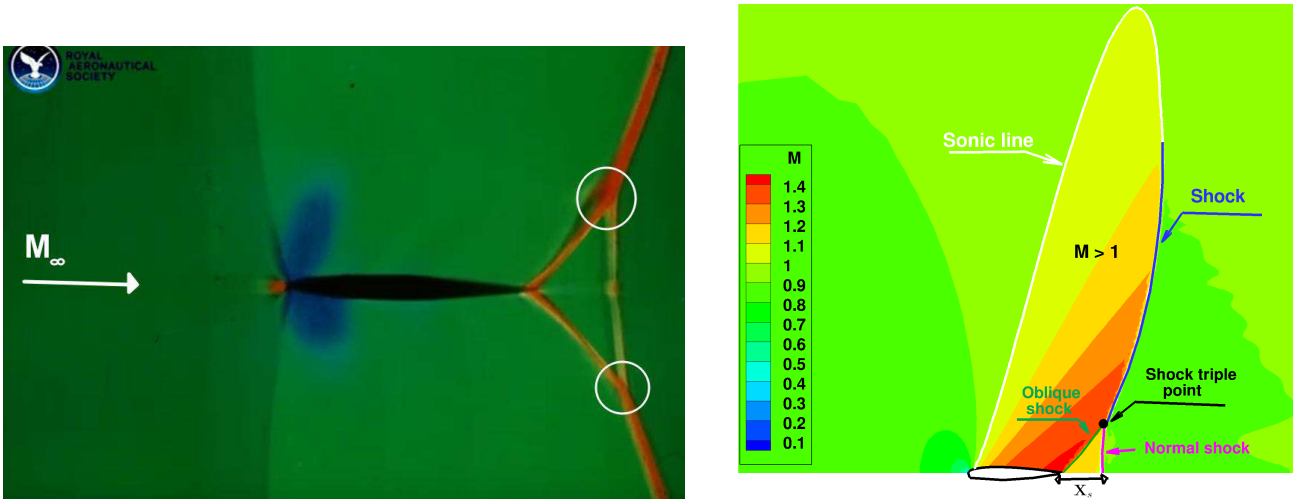

(a) Experimental visualization, re-printed from [8], with permission.

(b) Computed flow field around a NACA0012 airfoil at $M_\infty = 0.95$

Figure 1. Transonic flow past an airfoil and fishtail shock-structure

In recent work [6,7], we found that the conditions that prevail at the branching point of a fishtail shock-pattern are similar to those encountered in Mach reflections under the "von Neumann paradox" conditions. Indeed, making use of both shock-fitting and shock-capturing CFD simulations and classical shock-polar analysis, we found, at least for the range of boundary conditions and the geometry we examined, that the branching points observed in the fishtail shock-pattern cannot be analytically modeled using the 3ST, but the 4WT should be used instead.

In the present paper, we study the transonic flow in a two-dimensional planar channel featuring a lenticular bump on the lower wall. The geometry resembles the region close to the TE of an airfoil and the shock-pattern that arises is indeed very similar to the fishtail shock-structure we have previously described. One of the advantages in simulating an internal flow, as we do in this paper, is that it allows to use a much smaller computational domain than that required to simulate the external flow past an airfoil.

Numerical computations have been performed using two different CFD codes: the commercial shock-capturing code `CFD++` [18] and the in-house, open-source, shock-fitting code `UnDiFi-2D`, which has been developed by the authors [19].

The present study is organized as follows. Section 2 recalls both von Neumann's 3ST and Guderley's 4WT and also introduces the (M_1, σ_{12}) plane which allows to parametrically define the domain of existence of the 3ST and 4WT. Section 3 gives the definition of the test cases and analyses some interesting properties of both the 3ST and 4WT making use of both shock-capturing and shock-fitting simulations. Final considerations and remarks will be given in Section 4.

2. Generalities

2.1. *Shock-interaction modelling: three-shock theory (3ST) and four-wave theory (4WT)*

von Neumann's 3ST is used to analytically model the triple-point that occurs in Mach reflections (MR), see the sketch in Fig. 2a. The shock-pattern in the neighbourhood of the branching points of the fishtail shock-structure of Fig. 1a can also be described by borrowing the nomenclature used for Mach reflections. This is done in Fig. 2b, where the oblique shock emerging from the TE of the airfoil is the I-shock, which can be thought of as being "reflected" from the far field, thus giving rise to the nearly normal shocks (the R-shock). Beyond the branching point where the oblique and nearly normal shocks

interact, the former bends into the M-shock and the dashed line represents the contact-discontinuity or slip-stream (SS).

The non-linear algebraic equations governing the 3ST can be found in either [20, § 135] or [21, § 1.3.2] and consist in the Rankine-Hugoniot jump relations for all three shocks, supplemented by the condition of parallel streams and equal pressure across the contact discontinuity. The number of unknowns matches that of the available equations once three parameters are given. We assign: *i*) the adiabatic index, γ, of the gas (here always set equal to 1.4); *ii*) the Mach number, M_1, ahead of the I-shock and *iii*) a measure of the I-shock strength, which we here choose to be the I-shock angle, σ_{12}.

Solutions to the 3ST can be graphically found by seeking intersections between the I- and R-shock polar in the pressure-deflection (θ, ξ) plane, shown in the central frame of Figure 2; for given values of γ and M_1, an unique I-shock polar can be drawn.

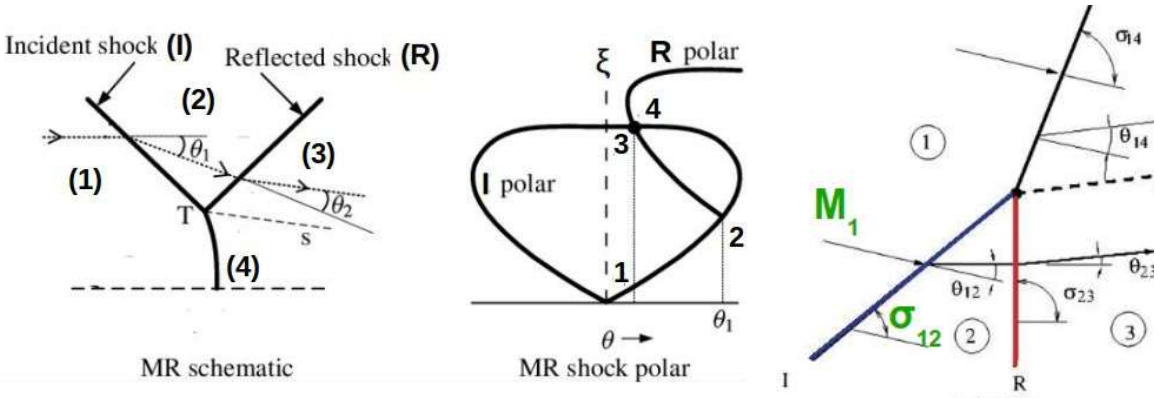

(a) Mach reflection schematic and corresponding shocks poplars (b) 3ST sketch

Figure 2. von Neumann's model (3ST)

Whenever the I- and R-shock polar do not intersect, as in Fig. 3a, von Neumann's 3ST has no solution and a different analytical model must be used. In [15,22] Guderley proposed the addition of a centred, isentropic expansion fan (EF) or Prandtl-Meyer (PM) wave that accelerates the flow from sonic conditions behind the R-shock to supersonic flow in region 5 of Fig. 3b. Guderley's model is commonly known as the four waves theory (4WT), the EF being the fourth wave; the 4WT was further modified by Khalghatgi and Hunt [23] by including a slip-stream, shown using a dashed line in Fig. 3b. Kalghatgi and Hunt [23] noticed that in region 4 of Fig. 3b, the flow can be either subsonic or supersonic; in the former case the flow pattern is referred to by [21] as a Vasil'ev reflection (VR), whereas in the latter as a Guderley reflection (GR).

The set of non-linear algebraic equations governing the 4WT is briefly recalled hereafter; the interested reader is referred to [16] for a more in-depth discussion. Given the free-stream Mach number, M_1 and I-shock angle, σ_{12}, which are the same two input parameters also used in the 3ST, the following quantities behind the I-shock can be easily computed: the flow deflection, θ_{12}, and pressure ratio, ξ_{21}, across the I-shock and the Mach number, M_2, in the region bounded by the I- and R-shocks. Since the flow behind the R-shock is sonic in the 4WT, i.e. $M_3 = 1$ in Fig. 3b, the R-shock angle, σ_{23}, can be computed from [24, Eq. (167)] using the known value of M_2. The pressure ratio across the R-shock, ξ_{32}, follows from [24, Eq. (128)] using the known values of M_2 and σ_{23}. The flow across the EF is isentropic, therefore:

$$\frac{p_5}{p_3} = \left[\frac{1+\delta\, M_5^2}{(\gamma+1)/2}\right]^{-\frac{\gamma}{\gamma-1}}$$

The two conditions that hold across the SS, i.e. equal flow direction and equal pressure, can be translated

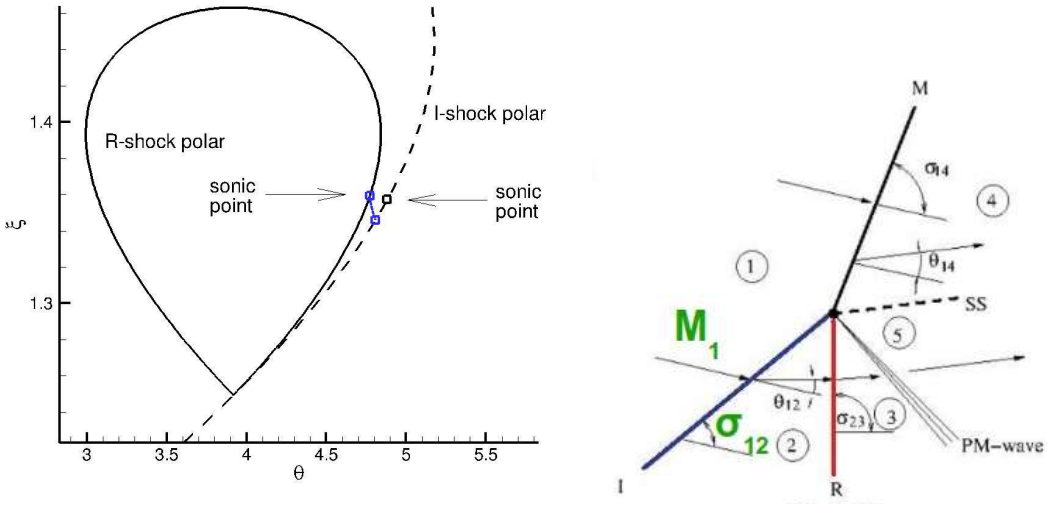

(a) Shock polar (b) 4WT sketch

Figure 3. Guderley's model (4WT)

into the following two by two non-linear system of algebraic equations:

$$\theta\left(M_1, \sigma_{14}\right) - \nu\left(M_5\right) = \theta_{12} + \theta_{23} \tag{1a}$$

$$\xi\left(M_1, \sigma_{14}\right)\left[\frac{1+\delta\, M_5^2}{(\gamma+1)/2}\right]^{\frac{\gamma}{\gamma-1}} = \xi_{32}\,\xi_{21} \tag{1b}$$

where terms in the r.h.s. are known and the only two unknowns appear on the l.h.s. These are: the (supersonic) Mach number, M_5, in the region bounded by the tail of the EF and the SS and the M-shock angle, σ_{14}. In Eqs. (1) θ and ξ are the flow deflection and pressure ratio through an oblique shock, which can be computed using [24, Eq. (138)] and [24, Eq. (128)], respectively; $\nu\left(M\right)$ is the Prandtl-Meyer function [24, Eq. (171c)].

2.2. *The* (M_1, σ_{12}) *plane*

A powerful graphical tool for looking at the existence and features of the solutions to both von Neumann's and Guderley's models consists in using a plane where the Mach number, M_1, upstream of the I-shock is on the x-axis and the I-shock local slope, σ_{12}, on the y-axis. The (M_1, σ_{12}) plane is drawn in Fig. 4, where we restrict the abscissas to the M_1-range that is relevant to the applications in § 3 and we only plot the curves which will be referred to throughout the paper. Using the same labeling as in [11], we draw:

- Line 1: where the incident shock (IS) is a Mach wave;
- Line 2: where the flow is sonic behind I-shock;
- Line 7a: marks the transition between the 3ST and 4WT and is characterized by sonic flow behind the R-shock in the 3ST;
- VR $\Leftrightarrow$ GR: marks the transition between the VR and GR and corresponds to sonic flow behind the M-shock in the 4WT.

The equations required to draw the aforementioned curves can be found in [6]. However, this is only a small subset of the numerous lines that bound regions of the (M_1, σ_{12}) plane where different shock-interaction patterns are observed. The interested reader is referred to [11,25–27] for a far more extensive discussion.

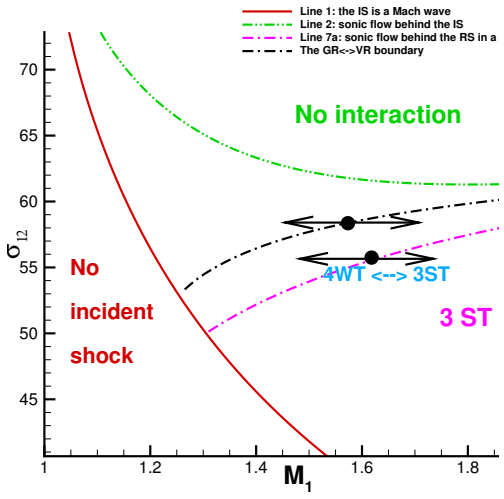

Figure 4. The (M_1, σ_{12}) plane

2.3. *CFD solvers*

The numerical simulations presented in this study have been carried out using two different CFD solvers. One is the commercial, shock-capturing code `CFD++` [18], which is widely used for simulating flows of aeronautical interest [28,29] on both structured and unstructured grids. The other is the in-house, shock-fitting code `UnDiFi-2D` which was developed by the authors [19] and is publicly accessible on the GitHub repository https://github.com/UnDiFi/UnDiFi-2D. `UnDiFi-2D` is capable of simulating shock/shock and shock/wall interactions in both steady and unsteady flows using 2D unstructured triangular grids; references [30–33] give examples of inviscid and viscous flow computations performed using `UnDiFi-2D` which highlight the main features of this shock-fitting technique as well as the advantages it offers over state-of-the-art shock-capturing codes when computing high-speed shocked-flows. In all numerical simulations performed using `UnDiFi-2D` in § 3 all shocks and slip-streams are fitted, i.e. treated as true mathematical discontinuities of zero thickness that bound regions of the flow field where a smooth solution to the governing PDEs exists; see [19,34,35] for algorithmic details. In addition, also those branching points where different discontinuities meet are treated as geometrical points (0-dimensional) and modeled as described in [30,36]. The available interaction models include the 3ST and 4WT, the latter being recently used to model the fishtail shock-pattern around the NACA0012 airfoil [6].

All numerical simulations included in this paper, performed either using `CFD++` or `UnDiFi-2D`, rely on second-order-accurate spatial discretization schemes. Whether the nominal order of accuracy of a numerical scheme can be preserved when shock waves are captured, will be discussed in § 3.1.

3. Test case definition

To investigate the properties of the fishtail shock-structure, we simulated the inviscid flow through the channel shown in Fig. 5a. The present test case has been carefully designed so as to allow the analytical or semi-analytical calculation of certain local and integral quantities. A uniform and weakly supersonic flow is prescribed along the inlet section of the duct, whereas a subsonic flow with a prescribed static pressure, P_{ex}, is set along the outflow section. The lower wall of the channel has the shape of a circular arc of radius $R = 10$ which subtends an angle $\alpha = 10°$, see Fig. 5a. A discontinuity in the slope of the lower wall is located at $(x, y)_{TE} = R\,(\sin\alpha, \cos\alpha - 1)$ where the circular arc joins the straight horizontal wall of the wider section of the channel. We shall hereafter refer to the aforementioned point as the trailing edge (TE) of the bump.

Table 1a gives an overview of the various flow configurations analyzed in this study: two groups of test cases (TC1 and TC2) have been defined according to the different inlet Mach number, M_{in}, whereas the lowercase letter identifies the prescribed exit-to-inlet static pressure ratio, P_{ex}/P_{in}.

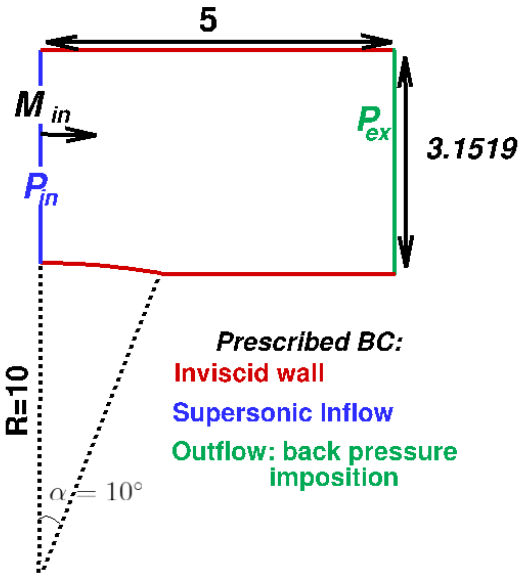

(a) Computational domain and boundary conditions

(b) Structured quadrilateral grids.

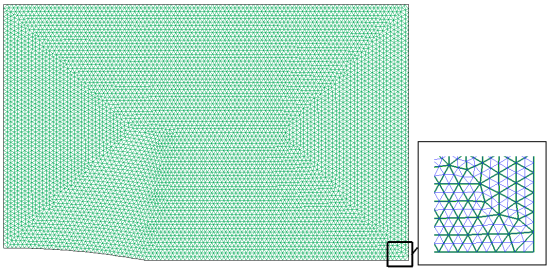

(c) Unstructured triangular grids.

Figure 5. Computational domain, boundary conditions and grids

Table 1. Boundary conditions defining the various test cases and global and local analytically computed quantities

(a) Labeling of the test cases

test case label	M_{in}	P_{ex}/P_{in}
TC1a	1.30	1.820
TC1b	1.30	1.819
TC1c	1.30	1.818
TC1d	1.30	1.817
TC1e	1.30	1.816
TC1f	1.30	1.815
TC2a	1.05	1.266
TC2b	1.05	1.265
TC2c	1.05	1.264

(b) Analytically computed quantities

	C_D	M_1	M_2	σ_{12}
TC1	0.0534	1.6443	1.2890	49.23°
			0.7052	80.00°
TC2	0.0786	1.4517	1.0351	60.86°
			0.8343	73.14°

The incoming supersonic flow expands and accelerates through the diverging part of the duct up to the TE where the slope discontinuity gives rise to an oblique shock wave, which can be either weak or strong, depending on the prescribed outflow pressure. A useful feature of the present testcase is highlighted in

	Structured grids		Unstructured grids	
Grid level	Nodes	Cells	Nodes	Cells
Coarse	6100	5940	7137	13954
Fine	24079	23760	28227	55816

Table 2. Features of the grids used

Fig. 6, where the Mach number distribution numerically calculated by solving the Euler equations is compared against the analytical, simple wave solution, of the flow past the lower wall of the channel. The comparison is limited to the trapezoidal region bounded in red, where the analytical solution is shown using red dashed iso-contour lines and the numerical one using black solid contour-lines. Excellent agreement between the two is observed close the lower wall, whereas the numerical solution deviates from the simple wave solution in regions where the two families of characteristic curves coexists. This is the case, for instance, close to the upper wall, where reflection of the incoming expansion wave occurs. Due to the higher inflow Mach number, the simple wave region covers a wider area for the TC1 inflow condition: compare Figs. 6a with 6b. For both sets of inflow conditions, however, the circular bump falls inside the simple wave region so that the Mach number distribution, $M(\theta)$, along the wall and up to the TE can be computed analytically using the Prandtl-Meyer function [24, Eq. (171)]. This, in turn, allows to compute the drag force by integrating along the circular arc the horizontal component of the pressure force exerted by the fluid on the wall:

$$D = R \int_0^{\alpha} P\,(\theta) \sin\theta \, d\theta \qquad \text{N/m} \tag{2a}$$

or, in dimensionless form, as:

$$C_D = \frac{D}{\frac{1}{2}\rho_{in}\, u_{in}^2\, \alpha\, R} = \frac{2}{\gamma\, M_{in}^2\, \alpha} \int_0^{\alpha} \frac{P(\theta)}{P_{in}} \sin\theta \, d\theta \tag{2b}$$

In Eqs. (2) θ is the angular coordinate of a cylindrical reference frame with the origin at the center of the circle in Fig. 5a and the static pressure distribution along the circular arc follows from the isentropic flow condition:

$$\frac{P(\theta)}{P_{in}} = \left(\frac{1 + \delta M_{in}^2}{1 + \delta M(\theta)^2} \right)^{\frac{\gamma}{\gamma-1}} \tag{3}$$

Even though the analytical value of static pressure can be computed using Eq. (3) all along the circular arc, the integral in Eqs. (2) must be numerically approximated. This has been accomplished using the `DGAUS8` routine from the `SLATEC` mathematical library [37] which guarantees an approximation error close to machine zero and therefore orders of magnitudes smaller than the discretization error incurred by second-order-accurate schemes, such as those employed here to discretize the governing PDEs. Therefore, the values so obtained from (2) can be regarded as "exact". Moreover, using the analytically computed Mach number at the TE, $M(\alpha) = M_1$, and the known flow deflection, α, through the oblique shock, it is possible to determine the shock slope at the TE using the oblique-shock relations. All the aforementioned analytically computed values are summarized in Tab. 1b where subscripts 1 and 2 refer to the shock-upstream, resp. downstream values at the TE. It is worth underlining that, as long as the oblique shock is attached to the TE of the bump, the flow along the bump is not affected by the prescribed outflow static pressure value, hence the drag and shock-upstream Mach number, M_1, in Tab. 1b take a unique value, regardless of the exit-to-inlet static pressure ratio. However, depending on the prescribed value of the outlet static pressure, the oblique shock at the TE can be strong or weak. In the former case, the shock-downstream flow is subsonic not only at the TE, but all along the curved shock wave which runs from the TE to the upper wall, see the TC1a flowfield in Fig. 8. When the outflow static pressure

is lowered, the oblique shock at the TE becomes weak, the downstream flow becomes supersonic and a shock-interaction resembling a λ-shock or fishtail shock-pattern appears. As the outflow pressure is further reduced, the interaction (or branching) point moves along the oblique shock towards the outflow section, see test cases TC1b to TC1f in Fig. 8.

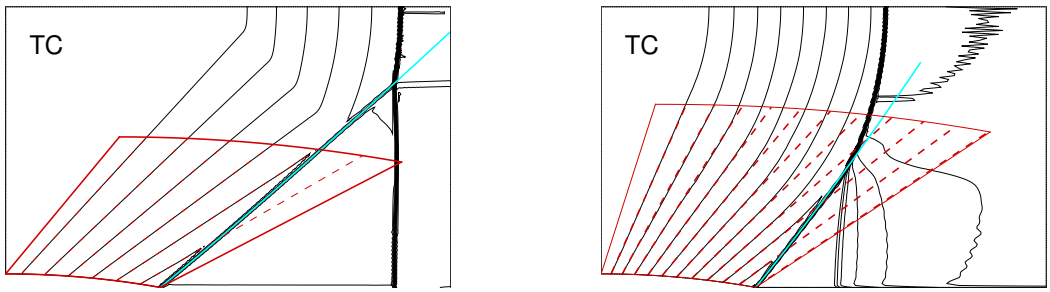

(a) TC1 (b) TC2

Figure 6. Comparison between the numerically computed Mach number distribution and the analytical simple wave solution.

Finally, since we are dealing with weak shocks of moderate intensity, it is possible to compute the shock shape using the semi-analytical, albeit approximate, approach described in [20, § 139]. The solid cyan lines drawn in Fig. 6 are the shock shapes computed by solving the ODE [20, Eq. (139.02)] using the `DDEABM` routine from `SLATEC` [37]: for both sets of test cases the agreement between the numerical and semi-analytical shock-shapes, starting at the TE and up to the branching point, is remarkably good. We will make use of the semi-analytical shock shape in Sects. 3.2 and 3.3 as an aid to assess whether the 3ST or 4WT applies at the branching point of the shock interaction.

As already mentioned, the flow patterns of Fig. 6 resemble the fishtail shock-pattern in the TE region of a profile flying at transonic speed and zero angle of attack: compare Figs. 1b and 6. However, compared to the external flow past the NACA0012 profile which we studied in [6], the chosen test case offers a twofold advantage. First of all, the possibility of varying both the inlet Mach number (M_{in}) and the pressure ratio between the exit and inlet sections, P_{ex}/P_{in}, allows to obtain a wide range of possible shock-interaction patterns. Secondly, numerical simulations of transonic external flows require a large computational domain owing to the relatively large size of the supersonic bubbles, see Fig. 1b, but also because the distance (X_s in Fig. 1b) between the nearly normal shock and the TE is very sensitive to the location of the far-field boundary [38]. The chosen internal flow test case can instead be computed using a small domain, thus reducing the computational cost. Despite this obvious advantage, the sensitivity of the computed shock-pattern to the boundary conditions was also observed in the proposed internal flow: tiny changes in the exit-to-inlet static pressure ratio give rise to major displacements of the shock-structure or even change the shock-topology. This feature makes code-to-code comparisons for the selected test case very difficult, because differences in the implementation of the constant pressure boundary condition in different codes turn out to be equivalent to tiny changes in the prescribed downstream pressure. This particular issue will be further addressed in § 3.1.

Both structured and unstructured grids, respectively shown in Fig. 5b and 5c, have been used to discretize the computational domain of Fig. 5a.

To evaluate the solution grid-independence, each test case was computed on two nested mesh levels, details of which are listed in Tab. 2. It is worth noting that, even if the structured and unstructured grids are characterized by a different number of nodes and cells, they share the same number and geometrical location of the gridpoints along the domain boundaries. The finest grid level was generated by recursively

subdividing each parent cell into four nested cells, as shown in the smaller frames of Figs. 5b and 5c.

3.1. *Grid convergence analysis*

Before analyzing the numerical solutions obtained using the two different CFD solvers, a grid-convergence analysis was performed. To do so, we use the TC1f case, which is characterized by a von Neumann interaction, as will be clarified in § 3.2. Figure 7a shows a sketch of the shock-pattern where the subsonic flow regions have been highlighted in gray.

Numerical simulations were computed using *i*) the `CFD++` code and the two nested structured grids shown in Fig. 5b and *ii*) the `UnDiFi-2D` code and the two unstructured grids shown in Fig. 5c. As mentioned earlier, code-to-code comparisons for the selected test case proved very difficult, because the two CFD codes return shock-patterns characterized by a different location of the branching point even when the same boundary conditions are prescribed. We argue that these differences are rooted in details of the implementation of the constant-pressure outflow boundary condition which are exacerbated by the extreme sensitivity of the computed shock-pattern to the prescribed outflow static pressure. Indeed, as will be shown in more details in § 3.2 and 3.3, even when using the same CFD code, changes as small as one-thousandth in the exit-to-inlet static pressure ratio cause a significant spatial displacement of the shock-pattern, or may even lead to a different shock-pattern. Therefore, when running the `UnDiFi-2D` shock-fitting calculations, instead of prescribing the same outflow pressure used in the `CFD++` calculation, we iteratively adjusted the outflow pressure to approximately obtain the same shock-location returned by `CFD++`. This is clearly a painful and time-consuming procedure[a], which explains why we have only run one shock-fitting calculation for each of the TC1 and TC2 sets of test cases.

Figures 7b and 7c compare the Mach iso-lines computed for the TC1f test case on both grids levels by `CFD++` and `UnDiFi-2D`, respectively. In the former case, the shock-capturing solutions obtained on the two mesh levels are in fair agreement, whereas an even better agreement can be seen for the `UnDiFi-2D` shock-fitting computations.

To quantitatively analyze the grid-convergence properties of the two different shock-modeling options, we need to compute the discretization error, i.e. the difference between the numerical and exact solution.

By reference to Fig. 7a, using the momentum conservation principle, it is easy to show that the drag coefficient, C_D, see Eq. (2b), can alternatively be computed as follows:

$$C_{D_{CFD}} = \frac{D_{CFD}}{\frac{1}{2}\rho_{in}u_{in}^2\alpha R} = \frac{1}{\frac{1}{2}\rho_{in}u_{in}^2\alpha R}\left[\int_0^{L_1}\left(p_{in}+\rho_{in}u_{in}^2\right)\,dy \;-\; \int_{R(\cos\alpha-1)}^{L_1}\left(p_{ex}+\rho_{ex}u_{ex}^2\right)\,dy\right] \tag{4}$$

where $L_1 = L_2 - R\,(1-\cos\alpha)$ and L_2 in Fig. 7a denote the height of the inlet and outlet sections of the channel. The first integral in Eq. (4) can be computed exactly, because it only depends on the uniform inlet conditions. The second integral is computed by numerically integrating the CFD solution along the exit section. By comparing C_D, computed using Eq. (2b) with the drag coefficient, $C_{D_{CFD}}$, computed using Eq. (4) and the `CFD++` and `UnDiFi-2D` numerical solutions on both grid levels, we can assess the grid-convergence-rate of the numerical solutions. Table 3 summarizes the results obtained from both codes using the two nested grid-levels; the relative percentage error:

$$\epsilon = \frac{C_{D_{CFD}} - C_D}{C_D}\cdot 100\% \tag{5}$$

is also shown. The relative error obtained from the `UnDiFi-2D` shock-fitting solution, ϵ_{SF}, is always lower than the error, ϵ_{SC}, obtained from the `CFD++` shock-capturing calculation; for example, ϵ_{SF} on the coarser mesh is lower than ϵ_{SC} on the finer mesh. We have also computed the measured order of accuracy, $\tilde{n}$, using the formulae given in [31,39], and found that $\tilde{n}$ is close to design order, $n = 2$, for the shock-fitting calculation, whereas it reduces below first order for the shock-capturing one. This observation points to

[a] It is even more so, because convergence to steady-state requires a huge number of iterations, regardless of the CFD code and pseudo-time integration strategy being used

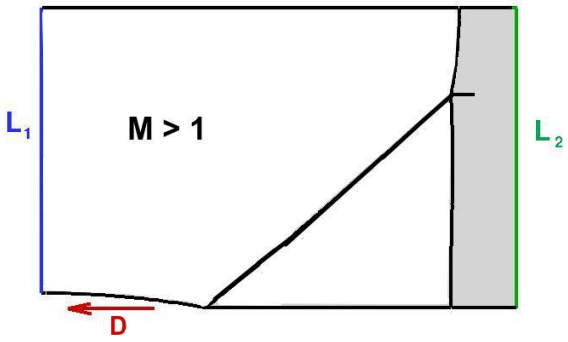

(a) Flow topology: gray regions denote subsonic flow

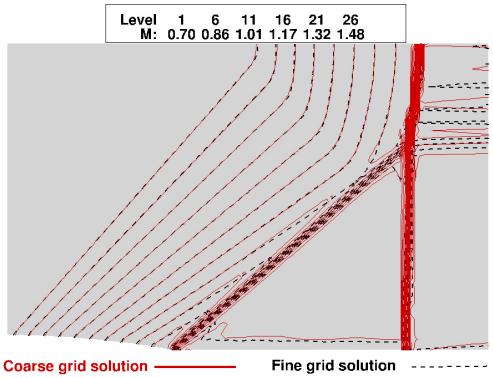

(b) `CFD++` solutions on nested structured grids.

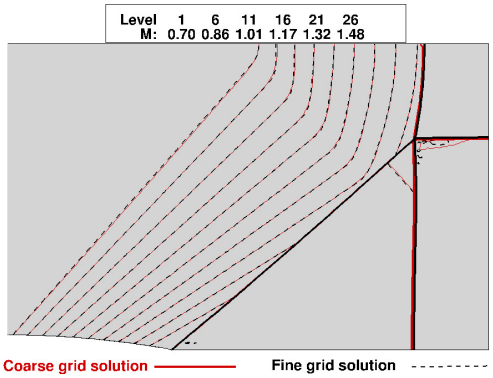

(c) `UnDiFi-2D` solutions on nested unstructured grids

Figure 7. Test case TC1f: flow topology and comparison between the Mach iso-contour lines computed using `CFD++` and `UnDiFi-2D` on both the coarse and fine meshes.

a well-known advantage of shock-fitting techniques over shock-capturing ones, namely the capability to retain the design order of accuracy also in the smooth flow regions located downstream of a discontinuity, see e.g. [31,33,40,41].

Both the qualitative and quantitative results presented so far point to the fact that the numerical solutions computed by both codes on the coarsest grid level are nearly grid-independent, the relative error on C_D being of the order of 1%.

	shock-fitting		shock-capturing	
Grid level	$C_{D_{CFD}}$	$\epsilon_{SF}(\%)$	$C_{D_{CFD}}$	$\epsilon_{SC}(\%)$
Coarse	0.0529	-0.936	0.0527	-1.311
Fine	0.0533	-0.187	0.0529	-0.936
$\tilde{n}$		2.32		0.49

Table 3. Drag estimate for TC1f case: comparison between the `CFD++` and `UnDiFi-2D` results.

3.2. *TC1 test cases*

In this paragraph we examine the six TC1 test cases, which share the same inlet Mach number, M_{in} = 1.3, whereas the exit-to-inlet static pressure ratio ranges between 1.820 and 1.815, see Tab. 1a. Figure 8 collects the Mach number contours computed for all six test cases using `CFD++` on the finest structured grid. The TC1f test case, which corresponds to P_{ex}/P_{in} = 1.815, was computed first. Then, the exit-to-inlet static pressure ratio was increased up to the value of the TC1e test case and the calculation was re-started from the TC1f solution and iterated until convergence to obtain the steady state solution of the TC1e case. This procedure was repeated to obtain the solutions of the remaining four test cases: TC1d was obtained using TC1e as initial condition and so on. We found by numerical experiments that the use of a different pseudo-transient approach for computing the various test cases may eventually lead to multiple

solutions for a given pair M_{in},P_{ex}/P_{in}; this statement will be made more precise later on. The sequence of frames in Fig. 8 shows the solutions computed with the aforementioned procedure and highlights how tiny variations in the pressure ratio, of the order of one thousandth, cause important changes in the flow topology. For example, the TC1a solution features a single strong curved shock originating at the TE, whereas all other test cases exhibit the fishtail shock-pattern. When gradually increasing the pressure ratio from TC1f to TC1b, the shock interaction moves upstream.

To determine which kind of interaction, whether a 3ST or a 4WT solution, characterizes each test case, we analyzed the numerical solutions and also made use of the semi-analytical shock-shape computed as described in § 3.

As far as the numerical approach is concerned, we extracted from the `CFD++` calculations the (M_1, σ_{12}) pairs close to the branching point and plotted them in the (M_1, σ_{12}) plane. More precisely, the Mach number, M_1, ahead of the I-shock is extracted directly from the CFD solutions, whereas the I-shock local slope, σ_{12}, is obtained from the computed pressure ratio across the I-shock. The points where data have been probed for each test case are marked in Fig. 8 using different symbols; there clearly is some ambiguity in the geometrical location of these points because in the shock-capturing calculation the branching point is not a geometrical point, but rather a region whose size is of the order of the numerical shock width. The TC1a test case has not been included in the analysis because for $P_{ex}/P_{in} = 1.820$ the oblique shock at the TE is a strong shock featuring subsonic shock-downstream flow and, therefore, no interaction takes place.

When using the semi-analytical approach, all (M_1,σ_{12}) pairs along the shock, i.e. the cyan line in Fig. 6a, are available, starting at the TE and moving away from the wall. The results are summarized in Fig. 9a were symbols have been used for the (M_1, σ_{12}) pairs extracted from the simulations and a solid line for the values obtained using the semi-analytical approach. The agreement between the two sets of results is extremely good for the largest values of the exit-to-inlet static pressure ratio, i.e. test cases TC1b-TC1d, but deteriorates when P_{ex}/P_{in} is lowered. This is because when the exit pressure is higher, see Fig. 8, the branching point is close to the TE and therefore inside the simple wave region. When the exit pressure decreases, the branching point moves along the oblique shock away from the TE, leaving the simple wave region, see Fig. 6a. The discrepancy arises from the fact that the semi-analytical model [20, § 139] is built upon the hypothesis that the shock-upstream flow is a simple wave. To further support our explanation, we have plot in Fig. 9b not only the (M_1,σ_{12}) pair at the branching point, but all pairs along the numerically simulated shock, starting at the TE and up to the triple point. It can be clearly seen that there is a perfect match with the semi-analytical solution close to the TE, whereas the numerical results deviate from the semi-analytical ones when the triple point is approached. The results shown in Fig. 9b refer to the TC1f test case, because it features a branching point that falls outside the simple wave region, see Figs. 7, 8 or 10.

Regardless of the approach used to characterize the interaction, Fig. 9a clearly reveals that all pairs of (M_1,σ_{12}) values fall in the region of the plane where von Neumann's 3ST has a valid solution. We therefore conclude that a von Neumann type interaction takes place in all five test cases TC1b to TC1f.

Once we have ascertained that in all five test cases featuring a fishtail shock-pattern the branching point should be modeled using von Neumann's 3ST, we have run a fully-fitted `UnDiFi-2D` simulation equipped with the 3ST to model the branching point; algorithmic details can be found in [36]. Figure 10 allows to compare the Mach number contours of the TC1f test case obtained using the two different shock-modeling options: shock-capturing in `CFD++` and shock-fitting in `UnDiFi-2D` on the finest grid level. Frames on the bottom row of Fig. 10 show a zoom centred around the branching point: the fitted discontinuities, all three shocks and the slip-stream, are marked using white solid lines. Both shock-modeling options are seen to be capable of identifying the three-shock confluence that characterizes von Neumann's model, sketched in Fig. 2b. The superior quality of the shock-fitting solution is however evident and it is due to the fact that all three shocks and the slip-stream are modeled as true mathematical discontinuities of zero thickness.

The availability of the flow variables on the two sides of the gas-dynamic discontinuities is yet another reason for using the shock-fitting technique to study these peculiar shock-patterns. Indeed, the shock-

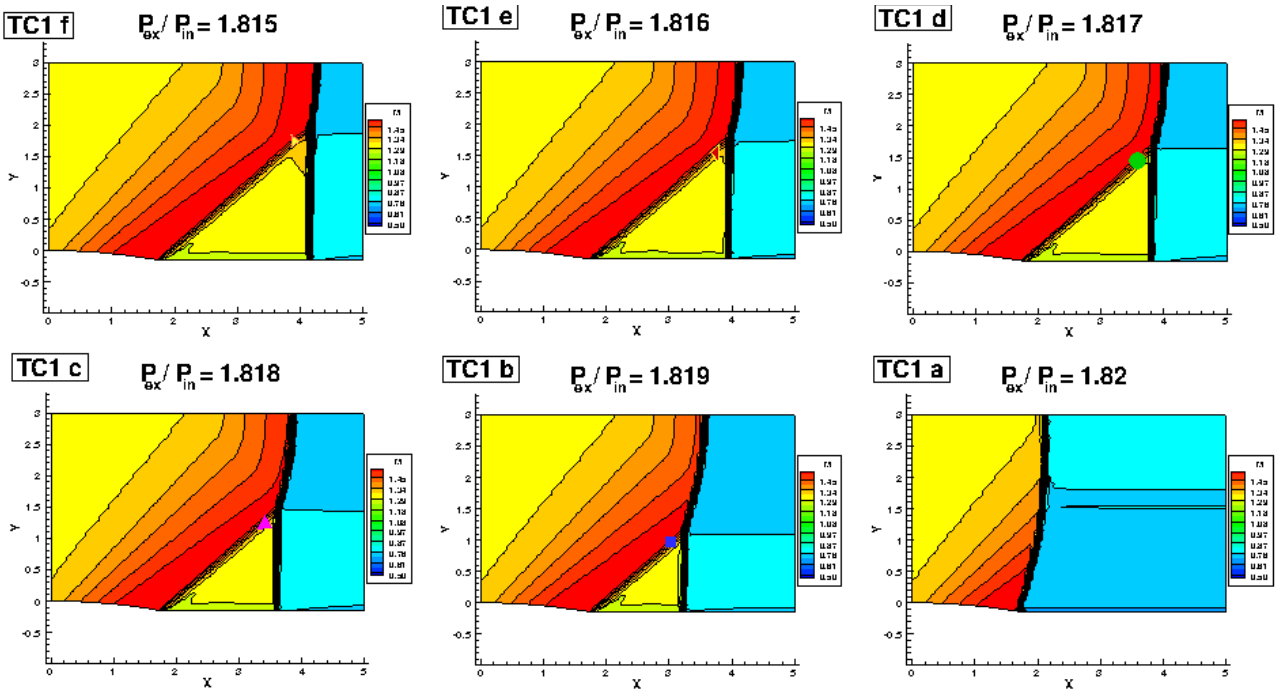

Figure 8. TC1 test cases ($M_{in} = 1.3$): evolution of the flow topology while increasing the exit-to-inlet static pressure ratio. CFD++ computations on the finest level of the structured grids.

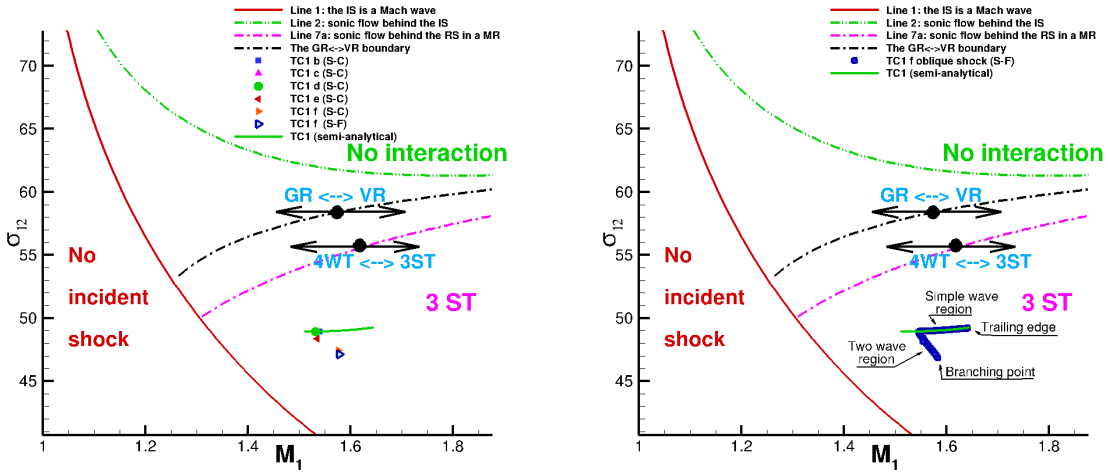

(a) TC1b-f test cases

(b) TC1f test case

Figure 9. TC1 test cases ($M_{in} = 1.3$): comparison between the numerical and semi-analytical results in the (M_1, σ_{12}) plane

fitting approach not only allows to know precisely the shock-upstream and downstream state, but also further information, such as the shock-shape, which is not immediately available in a shock-capturing solution. When comparing the data extracted from the shock-capturing and the shock-fitting solutions of the TC1f case, as we do in Fig. 9a, good agreement is found.

Figure 11 points to another interesting feature of these kind of flows. Let us consider the TC1d case ($P_{ex}/P_{in} = 1.817$), which is characterized by a von Neumann interaction, as shown in Fig. 8. If we use the TC1d solution as initial condition and reset the exit-to-inlet static pressure ratio to that of the TC1a test case, the simulation converges to the TC1a flow field shown in Fig. 8. However, if we now use the

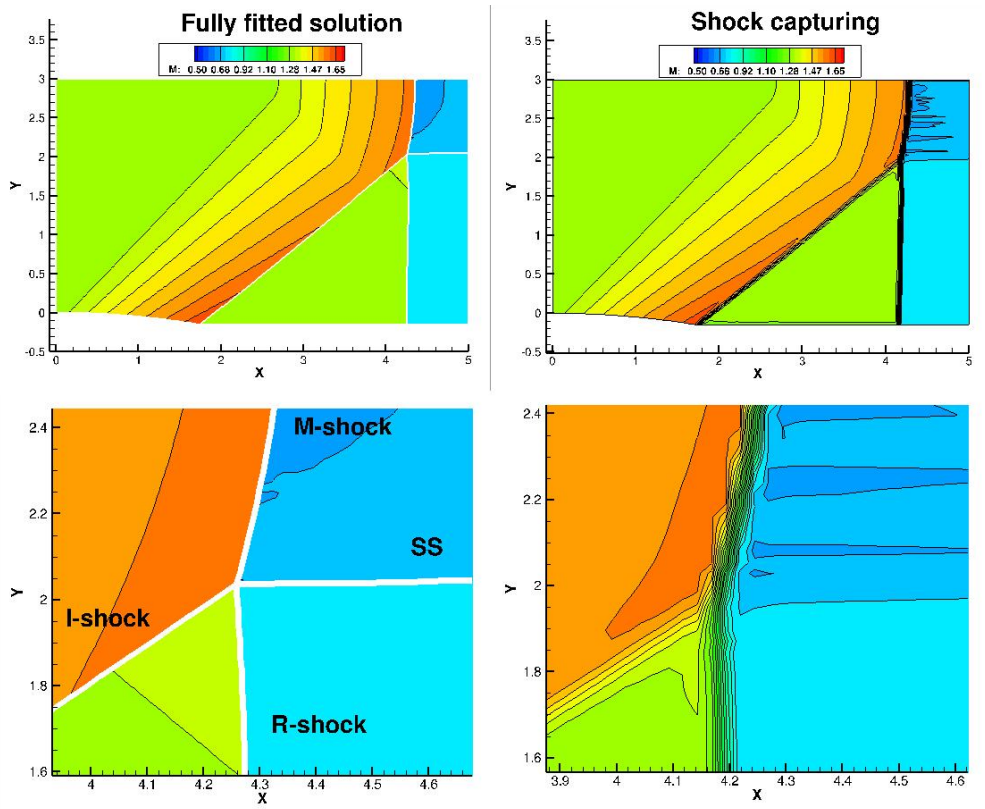

Figure 10. TC1f case: comparison between the Mach contours computed using `CFD++` and `UnDiFi-2D` on the finest grid level. Fitted discontinuities are shown using white solid lines.

TC1a solution as initial condition and restore the pressure boundary condition of the TC1d test case, i.e. $P_{ex}/P_{in} = 1.817$, the simulation converges to a topologically different steady-state, featuring a single strong curved shock and subsonic shock-downstream flow. This is illustrated in Fig. 11. In other words, the TC1d configuration admits two weak solutions of the Euler equations: depending on the transient, the flow field can be characterized by either a single strong shock wave originating at the TE or by a von Neumann interaction. The existence of multiple solutions was revealed also for TC1b and TC1d cases, corresponding to $P_{ex}/P_{in} = 1.819$ and $P_{ex}/P_{in} = 1.818$, respectively.

This phenomenon is similar to the hysteresis observed in the transition from Mach to regular reflection in steady flows that has been studied, both experimentally and numerically, by Ivanov and co-workers [42, 43]. More specifically, the transition from Mach to regular reflection in an over-expanded supersonic jet subjected to a varying pressure ratio exhibits a very similar behavior [44].

3.3. *TC2 test cases*

In this paragraph we analyze the TC2 cases which are characterized by a lower inlet Mach number, $M_{in} = 1.05$, than the TC1 test cases of § 3.2. Three different values of the exit-to-inlet static pressure ratio, see Tab. 1a, have been investigated using `CFD++` on the finest structured grid. The three frames of Fig. 12 show the numerical solutions obtained by increasing the pressure ratio from 1.264 to 1.266 and using the same procedure described in § 3.2. Figure 12 clearly highlights how tiny changes in the exit-to-inlet static pressure ratio significantly affect the overall flow field, eventually leading to a different shock-pattern. In all three cases a curved shock is attached to the TE of the bump. However, in the TC2a test case the shock is a strong shock with subsonic shock-downstream flow all the way from the TE to the upper wall of the channel, whereas in the other two test cases the curved shock starts at the TE as a weak oblique shock gradually becoming a normal shock as it reaches the upper wall. Therefore, shock interactions are only possible for the boundary conditions TC2b and TC2c. To identify the kind

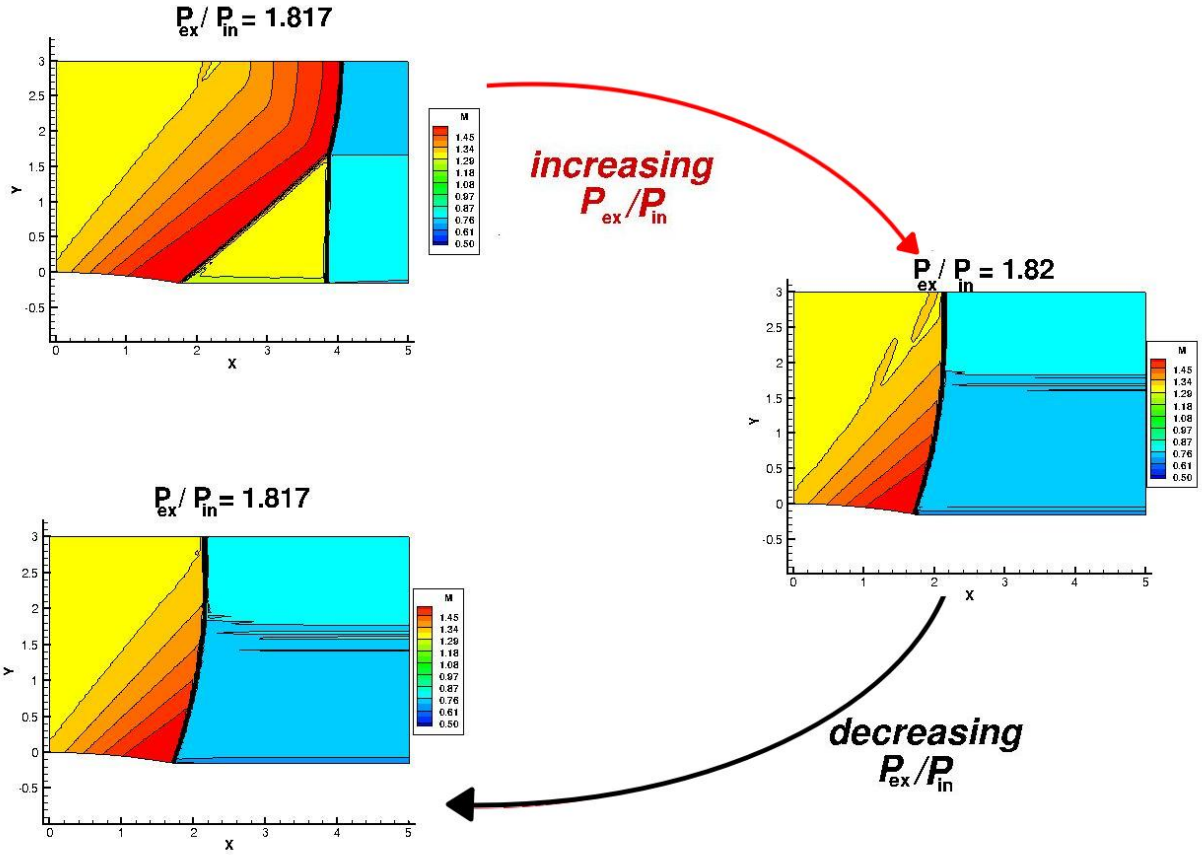

Figure 11. TC1d case: existence of multiple solutions for the same set of boundary conditions

of interaction that takes place in these two test cases, we plotted in Fig. 13b the two (M_1, σ_{12}) pairs probed from the `CFD++` shock-capturing calculation and also those available along the semi-analytical shock of Fig. 6b. These latter are shown using a solid line in Fig. 13b, whereas the results extracted from the simulations are shown using symbols. For the TC2 test cases, the agreement between the numerical and semi-analytical results is rather poor; this is because the flow ahead of the shock matches the simple wave solution only very close to the TE, see Fig. 6b, thus making the comparison with the semi-analytical solution of little use. Nonetheless, Fig. 13b shows that the two points representative of the TC2b and TC2c conditions fall inside the GR region, thus indicating that the branching point must be modeled according to the 4WT.

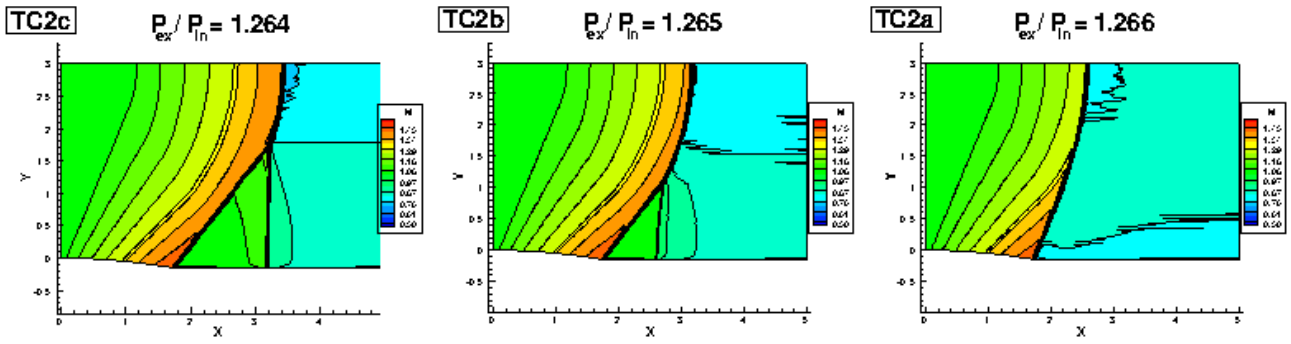

Figure 12. TC2 cases ($M_{in} = 1.05$): changes in flow topology while increasing the pressure ratio

A fully-fitted simulation of the TC2b test case, computed using `UnDiFi-2D` equipped with the 4WT model, is displayed in Fig. 13a. The fully-fitted simulation confirms that the branching point must be

modeled using the 4WT and allows to draw a more precise conclusion about the type of shock-interaction, whether a VR or GR, that takes place in the TC2b test case. The filled circle in Fig. 13b has been draw using the (M_1, σ_{12}) values at the branching point (QP in Fig. 14) of the fully-fitted simulation and confirms that the TC2b test case is characterized by a GR, featuring supersonic flow behind the M-shock.

Figure 14 shows a zoom centered around the branching point for both the shock-capturing (left) and shock-fitting (right) simulations. The latter closely matches the four-waves model sketched in Fig. 3b, whereas the shock-capturing calculation reveals a three-shocks confluence, but does not allow to identify the weak expansion fan that characterizes the GR. As shown in [45], a much finer grid resolution would be required, using shock-capturing, to identify the expansion fan.

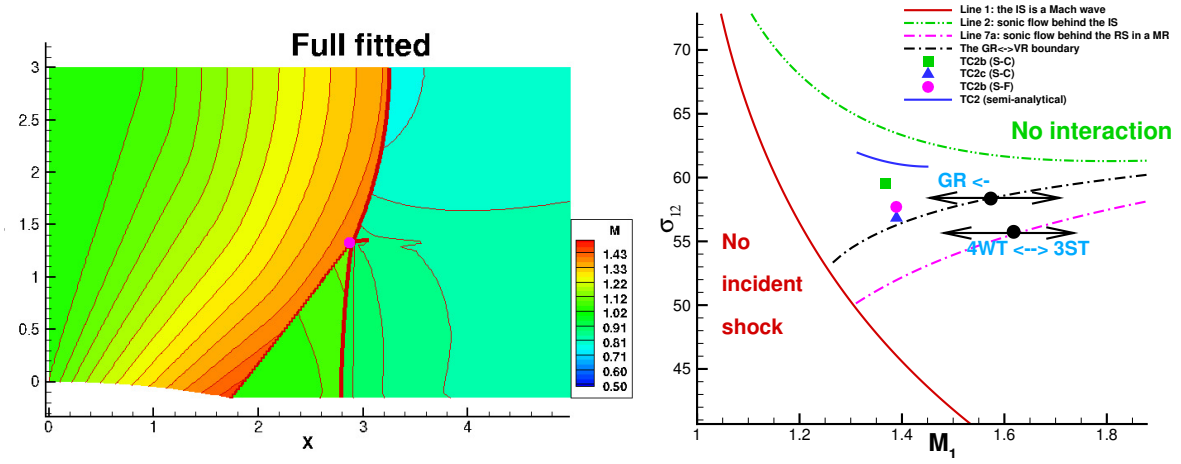

(a) Fully fitted computation: Mach flow field (b) The (M_1, σ_{12}) plane

Figure 13. TC2b case: fully fitted solution and analysis in the (M_1, σ_{12}) plane

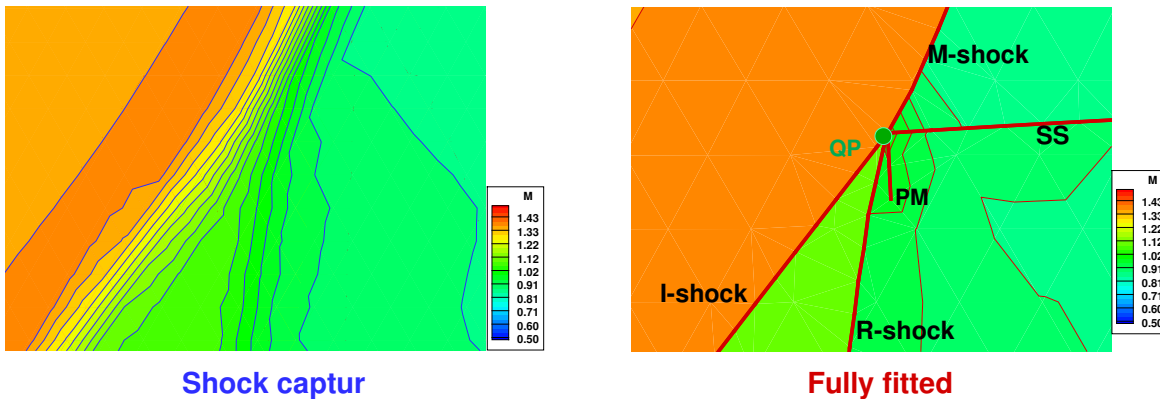

Figure 14. TC2b case: zoom centred at the branching point and comparison between the shock-capturing and fully fitted solutions

Finally, multiple solutions have also been found for the TC2 group of test cases, when using the same pseudo-time-stepping procedure described in § 3.2 for the TC1 test cases. In particular, Fig. 15 shows how the shock-topology changes when the outlet-to-inlet static pressure ratio, initially set to $P_{ex}/P_{in} = 1.264$, is first increased to $P_{ex}/P_{in} = 1.266$ (TC2a case) and then reset to its initial value.

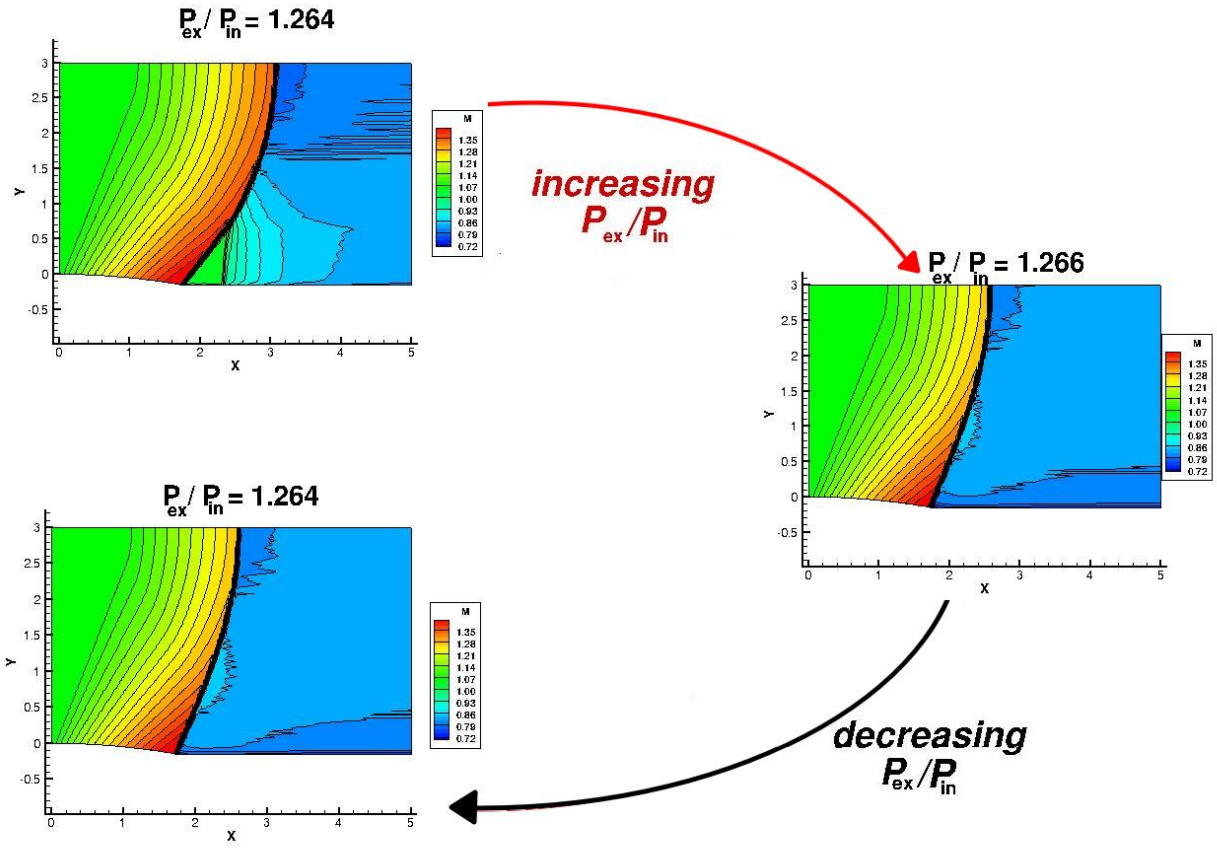

Figure 15. TC2c case: existence of multiple solutions for the same set of boundary conditions

4. Conclusions

In this work we studied the properties of the transonic flow in a planar channel featuring a lenticular bump on the lower wall. The chosen geometry, which closely resembles the region surrounding the TE of an airfoil at zero angle of attack, allows to investigate a wide range of shock-patterns by independently changing two boundary conditions: the inlet Mach number and the outlet-to-inlet static pressure ratio.

Numerical experiments have been conducted by solving the inviscid Euler equations using both a commercial and an in-house CFD code; discontinuities are modeled using the shock-capturing approach in the former and shock-fitting in the latter.

Depending on the selected pair of boundary conditions, we observed either a single curved shock attached to the geometrical discontinuity of the lower wall of the channel or a shock interaction that is reminiscent of the fishtail shock-pattern observed downstream of the TE of an airfoil flying at nearly sonic speed. Combining numerical simulations and shock-polar analysis, we conclude that when the inlet Mach number is only slightly above one, the branching point of the fishtail shock-pattern should be modeled using Guderley's four wave model, whereas for larger values of the inflow Mach number, von Neumann's three shock theory is applicable.

We have also observed that for some combinations of boundary conditions, two different steady-state shock topologies are observed, depending of the pseudo-transient evolution of the numerical simulation.

References

1. J. B. McDevitt, L. L. Levy Jr, and G. S. Deiwert, Transonic flow about a thick circular-arc airfoil, *AIAA Journal*, vol. 14, no. 5, pp. 606–613, 1976.
2. H. Tijdeman and R. Seebass, Transonic flow past oscillating airfoils, *Annual Review of Fluid Mechan-*

ics, vol. 12, no. 1, pp. 181–222, 1980.

3. B. Rasuo, An experimental and theoretical study of transonic flow about the NACA 0012 airfoil, in *24th AIAA Applied Aerodynamics Conference*, p. 3877, 2006.
4. V. Hermes, I. Klioutchnikov, and H. Olivier, Numerical investigation of unsteady wave phenomena for transonic airfoil flow, *Aerospace Science and Technology*, vol. 25, no. 1, pp. 224–233, 2013.
5. A. Jameson, Transonic flow calculations for aircraft, in *Numerical Methods in Fluid Dynamics: Lectures given at the 3rd 1983 Session of the Centro Internationale Matematico Estivo (CIME) held at Como, Italy, July 7–15, 1983*, pp. 156–242, Springer, 2006.
6. R. Paciorri, A. Bonfiglioli, and A. Assonitis, Features of "fishtail" shock interaction in transonic flows on a NACA0012 profile, *AIAA Journal*, 2024.
7. R. Paciorri, A. Bonfiglioli, and A. Assonitis, The transonic flow past a NACA0012 and the von Neumann paradox, in *AIAA Aviation 2022 Forum, Paper no. 2022–3990*, 2022.
8. Shell Film Unit, High speed flight: Part 2 - transonic flight. YouTube, 1959. uploaded by National Aerospace Library.
9. J. Von Neumann, Theory of shock waves, tech. rep., Institute for Advanced Study Princeton, NJ, 1943. also in: A. H. Taub (ed.), John von Neumann Collected Works, vol. VI: Theory of Games, Astrophysics, Hydrodynamics and Meteorology. Pergamon, 1963.
10. A. H. Taub, ed., *The Collected Works of John von Neumann: Volume VI: Theory of Games, Astrophysics, Hydrodynamics and Meteorology*. Pergamon Press, 1963.
11. C. J. Chapman, *High speed flow*. Cambridge University Press, 2000.
12. G. Birkhoff, *Hydrodynamics: A study in logic, fact, and similitude*. Princeton University Press, 1950.
13. P. Colella and L. F. Henderson, The von Neumann paradox for the diffraction of weak shock waves, *Journal of Fluid Mechanics*, vol. 213, pp. 71–94, 1990.
14. A. R. Zakharian, M. Brio, J. K. Hunter, and G. M. Webb, The von Neumann paradox in weak shock reflection, *Journal of Fluid Mechanics*, vol. 422, pp. 193–205, 2000.
15. K. G. Guderley, Considerations of the structure of mixed subsonic-supersonic flow patterns, Air Material Command Tech. Report, F-TR-2168-ND, ATI No. 22780, U.S. Wright-Patterson Air Force Base, GS-AAF-Wright Field 39, Dayton, Ohio, oct 1947.
16. E. I. Vasilev, T. Elperin, and G. Ben-Dor, Analytical reconsideration of the von Neumann paradox in the reflection of a shock wave over a wedge, *Physics of Fluids*, vol. 20, no. 4, p. 046101, 2008.
17. M. Ivanov, G. Shoev, D. Khotyanovsky, Y. Bondar, and A. Kudryavtsev, Supersonic patches in steady irregular reflection of weak shock waves, in *28th International Symposium on Shock Waves* (K. Kontis, ed.), pp. 543–548, Berlin: Springer, 2012.
18. S. Chakravarthy, O. Peroomian, U. Goldberg, and S. Palaniswamy, The CFD++ computational fluid dynamics software suite, in *AIAA and SAE, 1998 World Aviation Conference*, 1998.
19. L. Campoli, A. Assonitis, M. Ciallella, R. Paciorri, A. Bonfiglioli, and M. Ricchiuto, UnDiFi-2D: an unstructured discontinuity fitting code for 2D grids, *Computer Physics Communications*, vol. 271, p. 108202, 2022.
20. R. Courant and K. O. Friedrichs, *Supersonic Flow and Shock Waves*, vol. I of *Pure and Applied mathematics*. New York: Interscience Publishers, fourth ed., 1963.
21. G. Ben-Dor, *Shock wave reflection phenomena*. Springer Verlag, 2007.
22. K. G. Guderley, *Theory of Transonic Flow*. Pergamon Press, 1962.
23. G. T. Kalghatgi and B. L. Hunt, The three-shock confluence problem for normally impinging, over-expanded jets, *Aeronautical Quarterly*, vol. 26, no. 2, pp. 117–132, 1975.
24. Ames Research Staff, Equations, tables, and charts for compressible flow, tech. rep., NASA Ames Research Centre, 1953. NACA Report 1135.
25. H. Hornung, Regular and mach reflection of shock waves, *Annual Review of Fluid Mechanics*, vol. 18, no. 1, pp. 33–58, 1986.

26. C. A. Mouton, *Transition between Regular Reflection and Mach Reflection in the Dual-Solution Domain*. PhD thesis, California Institute of Technology, Pasadena, California, USA, 2007.
27. V. N. Uskov and M. V. Chernyshov, Special and extreme triple shock-wave configurations, *Journal of Applied Mechanics and Technical Physics*, vol. 47, pp. 492–504, 2006.
28. U. Goldberg and Y. Allaneau, Contribution from metacomp technologies, inc. to the second high lift prediction workshop, in *52nd Aerospace Sciences Meeting*, 2014.
29. S. Chakravarthy, D. Chi, and U. Goldberg, Flow prediction around the saccon configuration using CFD++, in *28th AIAA Applied Aerodynamics Conference*, 2010.
30. R. Paciorri and A. Bonfiglioli, Shock interaction computations on unstructured, two-dimensional grids using a shock-fitting technique, *Journal of Computational Physics*, vol. 230, no. 8, pp. 3155–3177, 2011.
31. A. Bonfiglioli and R. Paciorri, Convergence analysis of shock-capturing and shock-fitting solutions on unstructured grids, *AIAA Journal*, vol. 52, no. 7, pp. 1404–1416, 2014.
32. L. Campoli, P. Quemar, A. Bonfiglioli, and M. Ricchiuto, Shock-fitting and predictor-corrector explicit ale residual distribution, in *Shock Fitting: Classical Techniques, Recent Developments, and Memoirs of Gino Moretti* (M. Onofri and R. Paciorri, eds.), pp. 113–129, Cham: Springer International Publishing, 2017.
33. A. Assonitis, R. Paciorri, and A. Bonfiglioli, Numerical simulation of shock/boundary-layer interaction using an unstructured shock-fitting technique, *Computers & Fluids*, vol. 228, p. 105058, 2021.
34. R. Paciorri and A. Bonfiglioli, A shock-fitting technique for 2d unstructured grids, *Computers & Fluids*, vol. 38, no. 3, pp. 715–726, 2009.
35. A. Bonfiglioli, R. Paciorri, and L. Campoli, Unsteady shock-fitting for unstructured grids, *International Journal for Numerical Methods in Fluids*, vol. 81, no. 4, pp. 245–261, 2016.
36. M. S. Ivanov, A. Bonfiglioli, R. Paciorri, and F. Sabetta, Computation of weak steady shock reflections by means of an unstructured shock-fitting solver, *Shock Waves*, vol. 20, no. 4, pp. 271–284, 2010.
37. W. H. Vandevender and K. H. Haskell, The SLATEC mathematical subroutine library, *SIGNUM Newsl.*, vol. 17, pp. 16–21, sep 1982.
38. R. Richter and P. Leyland, Auto-adaptive finite element meshes, in *NASA Langley Research Center, ICASE/LaRC Workshop on Adaptive Grid Methods*, pp. 219–232, 1995.
39. P. J. Roache, Quantification of uncertainty in computational fluid dynamics, *Annual Review of Fluid Mechanics*, vol. 29, no. 1, pp. 123–160, 1997.
40. M. H. Carpenter and J. H. Casper, Accuracy of shock capturing in two spatial dimensions, *AIAA Journal*, vol. 37, no. 9, pp. 1072–1079, 1999.
41. A. Assonitis, R. Paciorri, M. Ciallella, M. Ricchiuto, and A. Bonfiglioli, Extrapolated shock fitting for two-dimensional flows on structured grids, *AIAA Journal*, vol. 60, no. 11, pp. 6301–6312, 2022.
42. M. S. Ivanov, D. Vandromme, V. Fomin, A. Kudryavtsev, A. Hadjadj, and D. Khotyanovsky, Transition between regular and Mach reflection of shock waves: new numerical and experimental results, *Shock Waves*, vol. 11, no. 3, pp. 199–207, 2001.
43. M. Ivanov, A. Kudryavtsev, S. Nikiforov, D. Khotyanovsky, and A. Pavlov, Experiments on shock wave reflection transition and hysteresis in low-noise wind tunnel, *Physics of Fluids*, vol. 15, no. 6, pp. 1807–1810, 2003.
44. A. Hadjadj, A. Kudryavtsev, and M. Ivanov, Numerical investigation of shock-reflection phenomena in overexpanded supersonic jets, *AIAA journal*, vol. 42, no. 3, pp. 570–577, 2004.
45. A. M. Tesdall, R. Sanders, and N. Popivanov, Further results on Guderley Mach reflection and the triple point paradox, *Journal of Scientific Computing*, vol. 64, no. 3, pp. 721–744, 2015.